

Cite this: *J. Mater. Chem. C*, 2023, **11**, 12900Received 5th July 2023,  
Accepted 16th September 2023

DOI: 10.1039/d3tc02370b

rsc.li/materials-c

# A narrow-bandgap non-fullerene acceptor constructed with an S,N-heteroacene up to a dodecamer in size†

Jiaxin Guo,<sup>‡</sup> Xinyuan Jia,<sup>‡</sup> Xiangjian Cao,<sup>a</sup> Tengfei He,<sup>c</sup> Huazhe Liang,<sup>a</sup> Wendi Shi,<sup>a</sup> Zheng Xu,<sup>a</sup> Ruohan Wang,<sup>a</sup> Yaxiao Guo,<sup>\*b</sup> Zhaoyang Yao,<sup>id</sup> <sup>\*a</sup> Xiangjian Wan,<sup>id</sup> <sup>a</sup> Guankui Long,<sup>id</sup> <sup>c</sup> Chenxi Li<sup>a</sup> and Yongsheng Chen<sup>id</sup> <sup>\*a</sup>

Two exotic non-fullerene acceptors (JX1 and JX2) were effectively developed, and were designed to include, respectively, decameric and dodecameric S,N-heteroacenes. The tandem coupling of electron-donating and electron-deficient moieties on the molecular skeleton enhanced intramolecular charge transfer dramatically, endowing specifically JX2 with excellent absorption of light of low energy approaching 1000 nm. Finally, a JX2-based device outputs a good PCE of 10.83%, providing a rare yet highly promising molecular platform for achieving efficient OSCs with near-infrared-II absorption.

## 1. Introduction

Organic solar cells (OSCs) constitute an emerging technology that is gaining extensive attention in the realm of sustainable energy.<sup>1–6</sup> To further speed up the development of OSCs, it is essential to investigate new active layer materials, especially non-fullerene acceptors (NFAs). Thus far, well-established NFAs such as Y6,<sup>8</sup> L8-BO,<sup>9</sup> BTP-eC9<sup>10</sup> and CH23<sup>11</sup> have contributed to power conversion efficiencies (PCEs) of OSCs beyond the remarkable threshold of 19%.<sup>12–16</sup> Since 52% of the total energy in standard solar spectra is contained in infrared (IR) absorption profiles, capturing the low-energy but abundant IR photons could constitute a feasible strategy for further boosting

the PCEs of OSCs.<sup>7,17</sup> In addition, NIR acceptors also have wide applications not only in tandem,<sup>18</sup> ternary,<sup>19</sup> and semi-transparent OSCs,<sup>20</sup> but also in other organic semiconductor devices such as high-performance NIR photodetectors,<sup>21</sup> etc.

Enhancing intramolecular charge transfer (ICT) by coupling strong donor units with strong acceptor units should be the basic strategy deployed for broadening the absorption ranges of light-harvesting molecules.<sup>22</sup> In particular, constructing highly electron-rich central donors consisting of large conjugated backbones would be expected to be very effective in this regard. Especially, both suitable energy levels and NIR absorptions can be achieved at the same time if the electron-donating and electron-deficient moieties are integrated into one ring-fused molecular framework. Moreover, the multi-level electron push-pull effect in such a unique architecture may also bring forth facilitated exciton/charge dynamics.<sup>23</sup>

In this regard, in the current work, two exotic NFAs, denoted as JX1 and JX2, have been effectively developed (Fig. 1a), and designed to include, respectively, decameric and dodecameric S,N-heteroacenes. The tandem coupling of electron-donating (thiophene and pyrrole) and electron-deficient (benzothiadiazole) moieties on the molecular skeleton was found to enhance ICT dramatically, resulting in an excellent absorption of light of low energy approaching 1.24 eV. Finally, the best-performing OSC based on JX2 showed a relatively good PCE of 10.83% and was featured with a photoelectric response at a wavelength of approaching 1000 nm.

## 2. Results and discussions

### 2.1. Theoretical calculations

We performed initial calculations, applying density functional theory (DFT), to determine optimized geometries and energy levels of JX1 and JX2 (Fig. 1b). Both JX1 and JX2 were calculated to adopt a rather planar conjugated backbone, a feature favourable for efficient ICT and intermolecular  $\pi$ - $\pi$  packings. The

<sup>a</sup> State Key Laboratory and Institute of Elemento-Organic Chemistry, The Centre of Nanoscale Science and Technology and Key Laboratory of Functional Polymer Materials, Renewable Energy Conversion and Storage Center (RECAST), College of Chemistry, Nankai University, Tianjin 300071, China.

E-mail: zyao@nankai.edu.cn, yschen99@nankai.edu.cn

<sup>b</sup> State Key Laboratory of Separation Membranes and Membrane Processes, School of Chemistry, Tiangong University, Tianjin 300387, China.

E-mail: yaxiaoguo@tiangong.edu.cn

<sup>c</sup> School of Materials Science and Engineering, National Institute for Advanced Materials, Renewable Energy Conversion and Storage Center (RECAST), Nankai University, 300350, Tianjin, China

† Electronic supplementary information (ESI) available. See DOI: <https://doi.org/10.1039/d3tc02370b>

‡ These authors contributed equally: Jiaxin Guo and Xinyuan Jia.

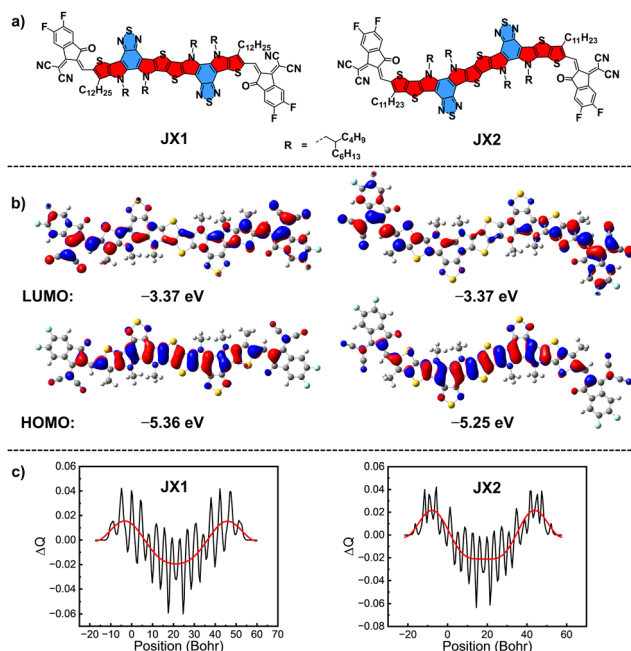


Fig. 1 (a) Molecular structures, (b) theoretical energy levels and frontier molecular orbital distributions, and (c) theoretical charge density difference ( $\Delta Q$ ) values along the backbones of **JX1** and **JX2**.<sup>7</sup>

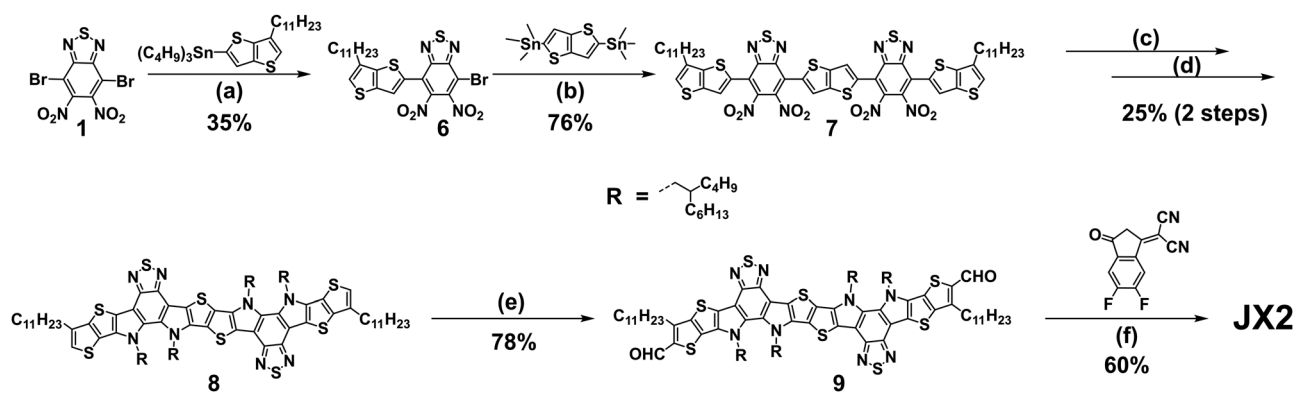
calculations also yielded the same lowest unoccupied molecular orbital (LUMO) energy level of  $-3.37$  eV for **JX1** and **JX2**, attributed to them having the same terminal units. Meanwhile, the highest occupied molecular orbital (HOMO) of **JX2** ( $-5.25$  eV) was observed to be upshifted compared to that of  $-5.36$  eV for **JX1**, attributed to the larger conjugated system of **JX2**. Moreover, in spite of the two-electron-deficient benzothiadiazole groups on the molecular skeletons of the central donor, both **JX1** and **JX2** were concluded, based on the  $\Delta Q$  plots displaying a peak-valley-peak shape<sup>7</sup> (Fig. 1c), to still possess a clear acceptor-donor-acceptor (A-D-A) character. Note, in general, that such a desirable A-D-A feature of an NFA is expected at least in theory to result in superior molecular packing, efficient exciton splitting, low energy losses and improved photovoltaic performances.<sup>7</sup>

## 2.2. Synthesis and characterization

Given the similar synthetic routes to **JX1** and **JX2**, we here describe the synthesis of just **JX2** (Scheme 1). The process started with a Stille coupling between **1** and tributyl (6-undecyl thieno [3,2-*b*]thiophen-2-yl) stannane to generate intermediate **6** in a moderate yield. This step was followed by further Stille coupling with 2,5-bis(trimethyl stannyl) thieno [3,2-*b*]thiophene to yield compound **7**. Then, the S,N-heteroacenes up to a dodecamer (**8**) was constructed through quadruple intramolecular Cadogan reductive cyclization by adding triphenylphosphine, followed by 5-(iodomethyl) undecane. Later, the dialdehyde compound **9** as a red powder was synthesized from **8** via the Vilsmeier-Haack reaction. Finally, the synthesis of the target **JX2** compound was accomplished by subjecting compound **9** and the end unit of 2FIC to a Knoevenagel condensation reaction.<sup>8</sup> The synthetic and characterization details are presented in Supplemental Experimental Procedures (Schemes S1, S2 and Fig. S12–S31, ESI<sup>†</sup>).

## 2.3. Optical and electrochemical properties

To experimentally determine the energy levels of the molecules, cyclic voltammetry (CV) was performed (Fig. S2, ESI<sup>†</sup>). Fig. 2a shows the LUMO/HOMO of **JX1** ( $-3.77/-5.41$  eV) and **JX2** ( $-3.79/-5.33$  eV), corresponding to band gaps of 1.64 and 1.54 eV, respectively. Due to the reduced band gap of **JX2**, it was reasonable to observe an obvious red-shift of the maximum absorption peaks for **JX2** in both solution and solid film, compared to those of **JX1** (Fig. 2b and Fig. S1, ESI<sup>†</sup>). As expected, **JX2** exhibited a red shift of approximately 17 nm in its solution absorption spectrum compared to that of **JX1**, with the maximum absorption peaks observed at 759 nm and 742 nm for **JX2** and **JX1**, respectively. Moreover, it's worth noting that the stronger absorption displayed by **JX2** than **JX1** in its solution absorption spectrum compared to that of **JX1**, with the maximum absorption peaks observed at 966 nm and 886 nm, respectively. The extended conjugation of the central donor of **JX2**, compared to that of **JX1**, was posited to account for the higher HOMO energy level of **JX2** and its red-shifted absorptions. The detailed physicochemical data are summarized in Table S1 (ESI<sup>†</sup>).



Scheme 1 Synthetic route to **JX2**. Reagents and conditions: (a) Pd<sub>2</sub>(dba)<sub>3</sub>, P(*o*-tolyl)<sub>3</sub>, toluene, 60 °C, 48 h; (b) Pd<sub>2</sub>(dba)<sub>3</sub>, P(*o*-tolyl)<sub>3</sub>, toluene, reflux, overnight; (c) PPh<sub>3</sub>, *o*-DCB, reflux, 12 h; (d) NaOH, DMF, 5-(iodomethyl)undecane, 90 °C, 72 h; (e) POCl<sub>3</sub>, DMF, ClCH<sub>2</sub>CH<sub>2</sub>Cl, reflux, 12 h; and (f) pyridine, CHCl<sub>3</sub>, reflux, 12 h.

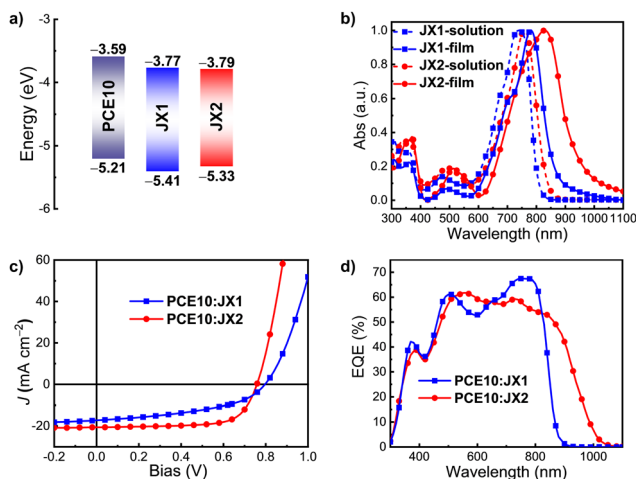


Fig. 2 (a) Plots of the energy level diagrams of PCE10, **JX1** and **JX2** neat films. (b) Normalized UV-Vis absorption spectra in solutions and thin films of **JX1** and **JX2**. (c)  $J$ - $V$  characteristics and (d) EQE spectra of devices based on **PCE10:JX1** and **PCE10:JX2**.

#### 2.4. Device characterization of OSCs

**JX1** and **JX2** were each blended with **PCE10**, a widely used polymer donor with matched HOMO and LUMO energy levels comparing to both **JX1** and **JX2** (Fig. S3, ESI<sup>†</sup>). The device optimizations are described in Supporting Information and detailed photovoltaic data are summarized in Tables S2–S6 (ESI<sup>†</sup>). Fig. 2c shows the best current density *versus* voltage ( $J$ - $V$ ) curves of the OSCs based on **PCE10:JX1** and **PCE10:JX2**. Here, an average PCE of 10.83% was reached by **JX2**-based OSCs, much better than the 6.24% value reached by its **JX1** counterparts, and was accompanied by a  $V_{OC}$  of 0.759 V,  $J_{SC}$  of 20.11 mA cm<sup>-2</sup> and FF of 69.56% (Table 1). The better performance of **JX2**-based OSCs, as compared to those based on **JX1**, can be primarily attributed to the higher  $J_{SC}$  and FF values displayed by the **JX2**-based OSCs. The improved  $J_{SC}$  of the **JX2**-based OSCs, in turn, can apparently be attributed mainly to the broader absorption, as displayed in the external quantum efficiency (EQE) curves (Fig. 2d) and also consistent with the absorption range of their blended films, shown in Fig. S4 (ESI<sup>†</sup>). The more ordered molecular packing of **JX2** was posited to be responsible for the greatly improved FF, as discussed below.

#### 2.5. Photodynamic analysis of OSCs

In order to elucidate the distinctions in EQEs and FFs between the **JX1**- and **JX2**-based OSCs, first the correlation between the photocurrent density ( $J_{ph}$ ) and effective voltage ( $V_{eff}$ ) was studied<sup>24</sup> (Fig. S5, ESI<sup>†</sup>). **JX2**-based OSCs afforded a superior exciton dissociation efficiency ( $P_{diss}$ ) of 95.6% and charge

collection efficiency ( $P_{coll}$ ) of 81.1%, compared to the 81.0%  $P_{diss}$  and 50.5%  $P_{coll}$  for the **JX1**-controlled OSCs. The higher  $P_{diss}$  and  $P_{coll}$  values for the **JX2**-based devices may be ascribed to their better nanoscale film morphology (discussed below) and resulting more balanced electron/hole mobility ratio<sup>25</sup> (Fig. 3a). In addition, measurements of the light intensity ( $P_{light}$ ) dependence for  $J_{SC}$  and  $V_{OC}$  were taken to investigate charge recombination kinetics in the OSCs. The  $\alpha$  values for **JX1**- and **JX2**-based devices were very similar and approached unity, indicating a significantly suppressed bimolecular recombination (Fig. S6a). Moreover, the slopes of the plots of  $(nkT/q)$  of  $V_{OC}$  *versus* the natural logarithm of  $P_{light}$  were measured to be 1.40 and 1.22  $kT/q$  for the **JX1**- and **JX2**-based devices, respectively (Fig. S6b, ESI<sup>†</sup>). The slightly smaller slope of the plot using **JX2** suggested fewer trap-assisted recombination losses.<sup>24,26</sup>

Photoluminescence (PL) quenching<sup>27</sup> experiments were also conducted to investigate the charge transfer occurring at the interfaces between the donor and acceptor materials. As shown in Fig. S7a and S7c (ESI<sup>†</sup>), the PL quenching efficiencies of **PCE10:JX1** blends were notably high, with values of 97.7% and 80.5% when compared to the neat **PCE10** and **JX1** films, respectively. However, the **PCE10:JX2** blends showed the same quenching efficiency of 97.7% when referring to neat **PCE10** films but a much lower quenching efficiency of 51.8% when referring to neat **JX2** films (Fig. S7b and S7d, ESI<sup>†</sup>). The inferior PL quenching efficiency of the **PCE10:JX2** blends when stimulating acceptor molecules may have been caused by the unshifted HOMO of **JX2**, which would have resulted in the decreased driving force for hole transfer. Then, transient photocurrent (TPC) and transient photovoltage (TPV) measurements<sup>28</sup> were taken to observe and analyse the charge extraction/recombination behaviours, respectively. The charge extraction times of **PCE10:JX1**- and **PCE10:JX2**-based devices were 0.35 and 0.18  $\mu$ s, respectively (Fig. 3b). Whereas the lifetimes of charge carriers in **JX1**- and **JX2**-based devices were determined to be 0.15 and 0.21 ms, respectively (Fig. 3c). These results were consistent with the relatively high FF values for **JX2**-based OSCs, and also suppressed trap-assisted recombination, as shown in Fig. S6b (ESI<sup>†</sup>).

#### 2.6. Morphology and energy loss analysis

In light of the critical importance of film morphology for achieving high-performance OSCs, atomic force microscopy (AFM)<sup>29</sup> along with grazing incident wide-angle X-ray scattering (GIWAXS) experiments<sup>30</sup> were carried out. As shown in Fig. 4a and b, the **PCE10:JX1**-based device exhibited a root-mean-square (RMS) roughness value of 0.70 nm, *i.e.*, considerably lower than the value of 1.84 nm observed for the **PCE10:JX2**-based device. This tendency

Table 1 Photovoltaic parameters of the optimal OSCs based on different active layers<sup>a</sup>

Active layer	$V_{OC}$ (V)	$J_{SC}$ (mA cm <sup>-2</sup> )	Calc. $J_{SC}^b$ (mA cm <sup>-2</sup> )	FF (%)	PCE (%)
<b>PCE10:JX1</b>	0.797 (0.794 ± 0.004)	17.46 (17.33 ± 0.27)	17.36	45.61 (44.90 ± 1.27)	6.24 (6.08 ± 0.29)
<b>PCE10:JX2</b>	0.759 (0.758 ± 0.002)	20.11 (20.08 ± 0.17)	19.27	69.56 (69.35 ± 0.41)	10.83 (10.72 ± 0.13)

<sup>a</sup> Statistical results from 10 OSCs are listed in parentheses. See Tables S5–S6 for the details. <sup>b</sup> Current densities derived from EQE plots.

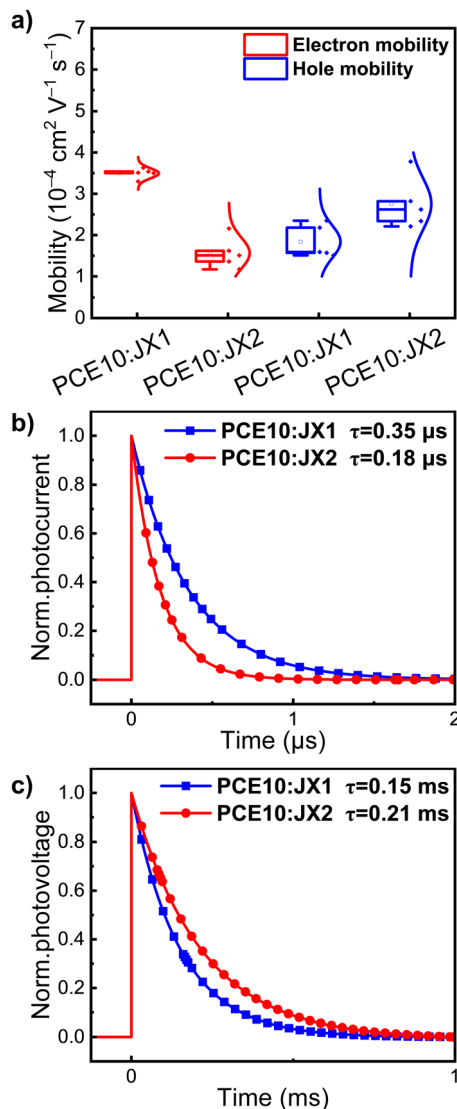


Fig. 3 (a) The statistic mobility values of OSCs based on **PCE10:JX1** and **PCE10:JX2** blends. (b) Transient photocurrent (TPC) and (c) transient photovoltage (TPV) measurements of devices based on **PCE10:JX1** and **PCE10:JX2**.

was also observed in the analysis of their phase images, shown in Fig. 4c, d and Fig. S8 (ESI<sup>†</sup>). The much larger but appropriate phase separation in the **PCE10:JX2** blend may have accounted for its facilitated charge transport and suppressed charge recombination, aligning with the conclusion we arrived at above. The 2D GIWAXS patterns acquired of the blended films are shown in Fig. S9b and S9d (ESI<sup>†</sup>). The resulting intensity profiles in the out-of-plane (OOP) and in-plane (IP) directions are presented in Fig. 4e and f. As summarized in Table S7 (ESI<sup>†</sup>), the (010) peaks of **PCE10:JX1** and **PCE10:JX2** in the OOP direction were both observed at similar positions, namely 1.64 and 1.66  $\text{\AA}^{-1}$ , which corresponded to  $\pi$ - $\pi$  stacking distance ( $d_{010}$ ) values of 3.84 and 3.79  $\text{\AA}$ , respectively. Moreover, the values of coherence length (CCL<sub>010</sub>) of  $\pi$ - $\pi$  stacking for **PCE10:JX1** and **PCE10:JX2** blends were calculated to be 7.73 and 9.68  $\text{\AA}$ , respectively. The slightly smaller  $d_{010}$  and greater CCL for the **PCE10:JX2** blends may be

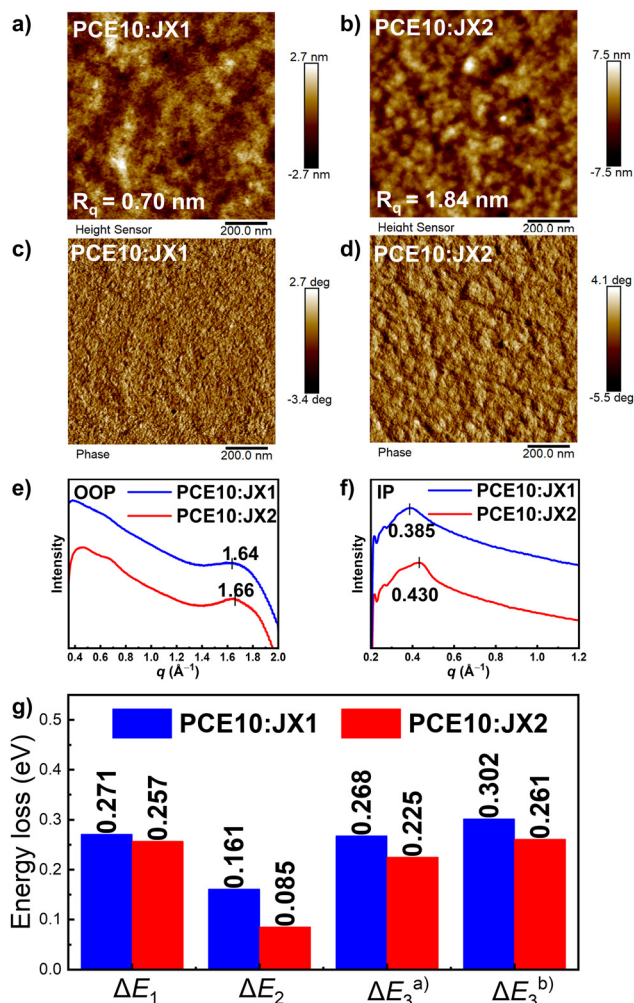


Fig. 4 (a) and (b) AFM height images. (c) and (d) AFM phase images. (e) and (f) 2D GIWAXS patterns and the corresponding OOP and IP line-cut profiles. (g)  $E_{\text{loss}}$  distributions of the corresponding devices.

ascribed to the stronger crystallinity of **JX2** caused by its relatively larger conjugated backbone, and further resulting in suppressed charge recombination. Note that the above variations in  $d_{010}$  and CCL were also in good agreement with those observed in their neat films (Fig. S9 and Table S7, ESI<sup>†</sup>).

As depicted in Fig. S10 (ESI<sup>†</sup>), the optical bandgap ( $E_g$ ) values of blended films were determined, by analysing the derivatives of the EQE curves,<sup>27,31</sup> to be 1.477 eV for **JX1** and 1.324 eV for **JX2**. The total energy loss ( $E_{\text{loss}}$ ) values of the OSCs were thus calculated to be 0.700 and 0.567 eV for **JX1** and **JX2**, respectively, demonstrating a significant reduction in  $E_{\text{loss}}$  after the utilization of an extended conjugated backbone for **JX2**. To deepen our understanding of the underlying causes of the  $E_{\text{loss}}$ , all three parts of  $E_{\text{loss}}$  were evaluated and are illustrated in Fig. 4g. The detailed calculation method for the three parts is provided in Note S1. Regarding these three parts of  $E_{\text{loss}}$ , in general  $\Delta E_3$  indicates the non-radiative energy loss, which is of the most concern in current high-performance OSCs. Note, in the current work, that a lower value of  $\Delta E_3$  (0.225 eV) was attained by **PCE10:JX2**-based OSCs than by a tested **PCE10:JX1**-based one

(0.268 eV). Although some discrepancy can be usually observed for  $\Delta E_3$ , values obtained using different methods, the pattern of  $\Delta E_3$  values agreed well with the values estimated from EQE<sub>EL</sub> (Fig. S11, ESI†).<sup>32</sup> Note that the suppressed non-radiative recombination may be attributed to the superior nanoscale film morphology for the PCE10:JX2 blends, and apparently contributed to its improved photovoltaic parameters.

### 3. Conclusions

In order to maximize the utilization of low-energy photons in solar light, two NIR-absorbing, structurally exotic NFAs, denoted as JX1 and JX2, have been effectively developed and designed to include, respectively, decameric and dodecameric S,N-heteroacenes. The tandem coupling of electron-donating and electron-deficient moieties on the molecular skeleton enhanced the intramolecular charge transfer dramatically, endowing specifically JX2 with excellent absorption of light of low energy approaching 1000 nm. A systematic investigation showed that, compared to JX1-based OSCs, JX2-based OSCs displayed more efficient charge generation/transport and suppressed charge recombination due to superior film morphology. As a result, the tested JX2-based OSCs output a PCE, at 10.83%, better than the 6.24% PCE output by the tested JX1-based devices. Our work has not only provided a rare yet highly promising molecular platform with NIR absorption, but is expected to stimulate the investigation of novel S,N-heteroacenes involving the coupling of multiple electron-donating and electron-deficient moieties into one molecular skeleton, with the aim of further improving photovoltaic performances of OSCs.

### Author contributions

J. G. synthesized materials and wrote the original paper. X. J. conducted the device optimization. G. L. and T. H. carried out the theoretical computations. X. C. and H. L. performed the EL and sEQE experiments. W. S., Z. X. and R. W. helped to analyse the data. C. L. and X. W. helped to analyse the data and revise the manuscript. Y. G., Z. Y. and Y. C. supervised and directed this project. All authors discussed the results and commented on the manuscript.

### Conflicts of interest

The authors declare no conflict of interest.

### Acknowledgements

The authors gratefully acknowledge the financial support from MoST (National Key R&D Program of China, 2022YFB4200400, 2019YFA0705900) of China and NSFC (21935007, 52025033, 22204119), Tianjin city (22JCQJNC00530).

### References

- X. Rodriguez-Martinez, S. Riera-Galindo, J. Cong, T. Osterberg, M. Campoy-Quiles and O. Inganäs, *J. Mater. Chem. A*, 2022, **10**, 10768–10779.
- G. Yu, J. Gao, J. C. Hummelen, F. Wudl and A. J. Heeger, *Science*, 1995, **270**, 1789–1791.
- L. Zhu, M. Zhang, J. Xu, C. Li, J. Yan, G. Zhou, W. Zhong, T. Hao, J. Song, X. Xue, Z. Zhou, R. Zeng, H. Zhu, C. C. Chen, R. C. I. MacKenzie, Y. Zou, J. Nelson, Y. Zhang, Y. Sun and F. Liu, *Nat. Mater.*, 2022, **21**, 656–663.
- Y. Cui, Y. Xu, H. Yao, P. Bi, L. Hong, J. Zhang, Y. Zu, T. Zhang, J. Qin, J. Ren, Z. Chen, C. He, X. Hao, Z. Wei and J. Hou, *Adv. Mater.*, 2021, **33**, e2102420.
- Y. C. Liang, D. F. Zhang, Z. R. Wu, T. Jia, L. Luer, H. R. Tang, L. Hong, J. B. Zhang, K. Zhang, C. J. Brabec, N. Li and F. Huang, *Nat. Energy*, 2022, **7**, 1180–1190.
- M. Zhang, L. Zhu, G. Zhou, T. Hao, C. Qiu, Z. Zhao, Q. Hu, B. W. Larson, H. Zhu, Z. Ma, Z. Tang, W. Feng, Y. Zhang, T. P. Russell and F. Liu, *Nat. Commun.*, 2021, **12**, 309.
- X. Wan, C. Li, M. Zhang and Y. Chen, *Chem. Soc. Rev.*, 2020, **49**, 2828–2842.
- J. Yuan, Y. Zhang, L. Zhou, G. Zhang, H.-L. Yip, T.-K. Lau, X. Lu, C. Zhu, H. Peng, P. A. Johnson, M. Leclerc, Y. Cao, J. Ulanski, Y. Li and Y. Zou, *Joule*, 2019, **3**, 1140–1151.
- C. Li, J. Zhou, J. Song, J. Xu, H. Zhang, X. Zhang, J. Guo, L. Zhu, D. Wei, G. Han, J. Min, Y. Zhang, Z. Xie, Y. Yi, H. Yan, F. Gao, F. Liu and Y. Sun, *Nat. Energy*, 2021, **6**, 605–613.
- Y. Cui, H. Yao, J. Zhang, K. Xian, T. Zhang, L. Hong, Y. Wang, Y. Xu, K. Ma, C. An, C. He, Z. Wei, F. Gao and J. Hou, *Adv. Mater.*, 2020, **32**, e1908205.
- H. Liang, H. Chen, P. Wang, Y. Zhu, Y. Zhang, W. Feng, K. Ma, Y. Lin, Z. Ma, G. Long, C. Li, B. Kan, Z. Yao, H. Zhang, X. Wan and Y. Chen, *Adv. Funct. Mater.*, 2023, **33**, 2301573.
- W. Gao, F. Qi, Z. Peng, F. R. Lin, K. Jiang, C. Zhong, W. Kaminsky, Z. Guan, C. S. Lee, T. J. Marks, H. Ade and A. K. Jen, *Adv. Mater.*, 2022, **34**, e2202089.
- S. Li, C. He, T. Chen, J. Zheng, R. Sun, J. Fang, Y. Chen, Y. Pan, K. Yan, C.-Z. Li, M. Shi, L. Zuo, C.-Q. Ma, J. Min, Y. Liu and H. Chen, *Energy Environ. Sci.*, 2023, **16**, 2262–2273.
- Z. Chen, H. Yao, J. Wang, J. Zhang, T. Zhang, Z. Li, J. Qiao, S. Xiu, X. Hao and J. Hou, *Energy Environ. Sci.*, 2023, **16**, 2637–2645.
- L. Zhan, S. Li, Y. Li, R. Sun, J. Min, Z. Bi, W. Ma, Z. Chen, G. Zhou, H. Zhu, M. Shi, L. Zuo and H. Chen, *Joule*, 2022, **6**, 662–675.
- Y. Wei, Z. Chen, G. Lu, N. Yu, C. Li, J. Gao, X. Gu, X. Hao, G. Lu, Z. Tang, J. Zhang, Z. Wei, X. Zhang and H. Huang, *Adv. Mater.*, 2022, **34**, e2204718.
- L. Meng, Y. Zhang, X. Wan, C. Li, X. Zhang, Y. Wang, X. Ke, Z. Xiao, L. Ding, R. Xia, H. L. Yip, Y. Cao and Y. Chen, *Science*, 2018, **361**, 1094–1098.
- H. H. Gao, Y. N. Sun, Y. Cai, X. J. Wan, L. X. Meng, X. Ke, S. T. Li, Y. M. Zhang, R. X. Xia, N. Zheng, Z. Q. Xie, C. X. Li, M. T. Zhang, H. L. Yip, Y. Cao and Y. S. Chen, *Adv. Energy Mater.*, 2019, **9**, 1901024.

- 19 T. Liu, Z. Luo, Y. Chen, T. Yang, Y. Xiao, G. Zhang, R. Ma, X. Lu, C. Zhan, M. Zhang, C. Yang, Y. Li, J. Yao and H. Yan, *Energy Environ. Sci.*, 2019, **12**, 2529–2536.
- 20 D. Wang, H. R. Liu, Y. H. Li, G. Q. Zhou, L. L. Zhan, H. M. Zhu, X. H. Lu, H. Z. Chen and C. Z. Li, *Joule*, 2021, **5**, 945–957.
- 21 Y. Chen, Y. Zheng, Y. Jiang, H. Fan and X. Zhu, *J. Am. Chem. Soc.*, 2021, **143**, 4281–4289.
- 22 J. Zyss, I. Ledoux, S. Volkov, V. Chernyak, S. Mukamel, G. P. Bartholomew and G. C. Bazan, *J. Am. Chem. Soc.*, 2000, **122**, 11956–11962.
- 23 A. Barak, N. Dhiman, F. Sturm, F. Rauch, Y. A. Lakshmana, K. S. Findlay, A. Beeby, T. B. Marder and S. Umaphathy, *ChemPhotoChem*, 2022, **6**, e202200146.
- 24 A. K. Kyaw, D. H. Wang, V. Gupta, W. L. Leong, L. Ke, G. C. Bazan and A. J. Heeger, *ACS Nano*, 2013, **7**, 4569–4577.
- 25 X. N. Zhang, C. Li, J. Q. Xu, R. Wang, J. L. Song, H. Zhang, Y. X. Li, Y. N. Jing, S. L. Li, G. B. Wu, J. Zhou, X. Li, Y. Y. Zhang, X. Li, J. Q. Zhang, C. F. Zhang, H. Q. Zhou, Y. M. Sun and Y. Zhang, *Joule*, 2022, **6**, 444–457.
- 26 L. J. A. Koster, V. D. Mihailetschi, R. Ramaker and P. W. M. Blom, *Appl. Phys. Lett.*, 2005, **86**, 123509.
- 27 Y. M. Wang, D. P. Qian, Y. Cui, H. T. Zhang, J. H. Hou, K. Vandewal, T. Kirchartz and F. Gao, *Adv. Energy Mater.*, 2018, **8**, 1801352.
- 28 Y. Chen, F. Bai, Z. Peng, L. Zhu, J. Zhang, X. Zou, Y. Qin, H. K. Kim, J. Yuan, L. K. Ma, J. Zhang, H. Yu, P. C. Y. Chow, F. Huang, Y. Zou, H. Ade, F. Liu and H. Yan, *Adv. Energy Mater.*, 2020, **11**, 2003141.
- 29 Y. Huang, E. J. Kramer, A. J. Heeger and G. C. Bazan, *Chem. Rev.*, 2014, **114**, 7006–7043.
- 30 P. Müller-Buschbaum, *Adv. Mater.*, 2014, **26**, 7692–7709.
- 31 U. Rau, B. Blank, T. C. M. Muller and T. Kirchartz, *Phys. Rev. Appl.*, 2017, **7**, 044016.
- 32 X. K. Chen, D. P. Qian, Y. M. Wang, T. Kirchartz, W. Tress, H. F. Yao, J. Yuan, M. Hulsbeck, M. J. Zhang, Y. P. Zou, Y. M. Sun, Y. F. Li, J. H. Hou, O. Inganäs, V. Coropceanu, J. L. Bredas and F. Gao, *Nat. Energy*, 2021, **6**, 799–806.